

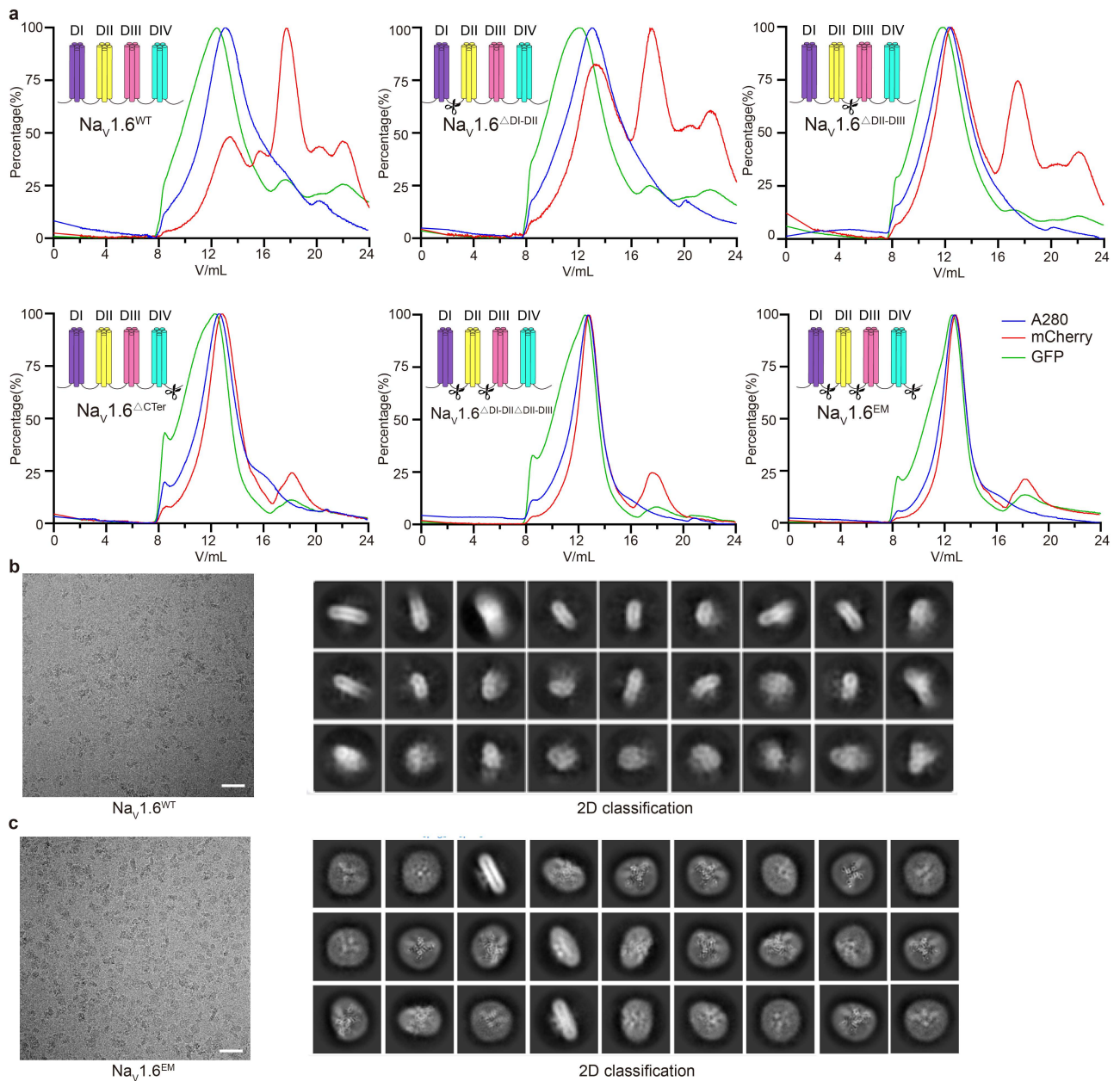
Supplementary Information for

Structure of human Nav1.6 channel reveals Na⁺ selectivity and pore blockade by 4,9-anhydro-tetrodotoxin

Authors

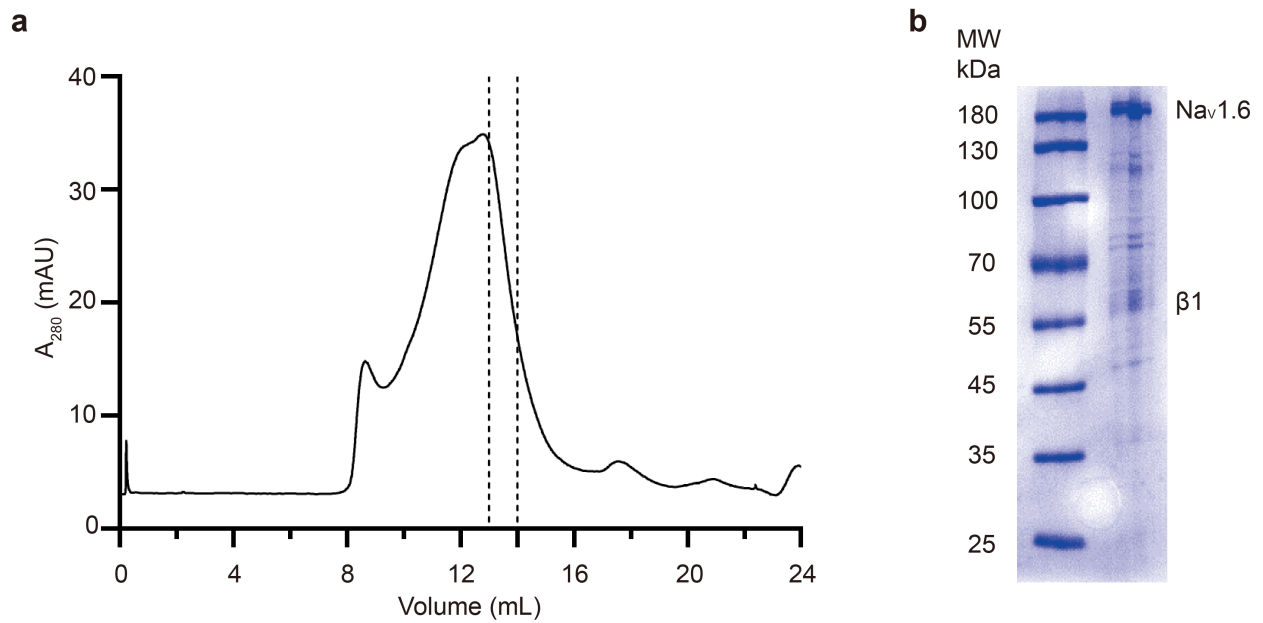
Yue Li, Tian Yuan, Bo Huang, Feng Zhou, Chao Peng, Xiaojing Li, Yunlong Qiu, Bei Yang, Yan Zhao, Zhuo Huang, Daohua Jiang

This file contains Supplementary Figure 1-10 and Table 1-3.



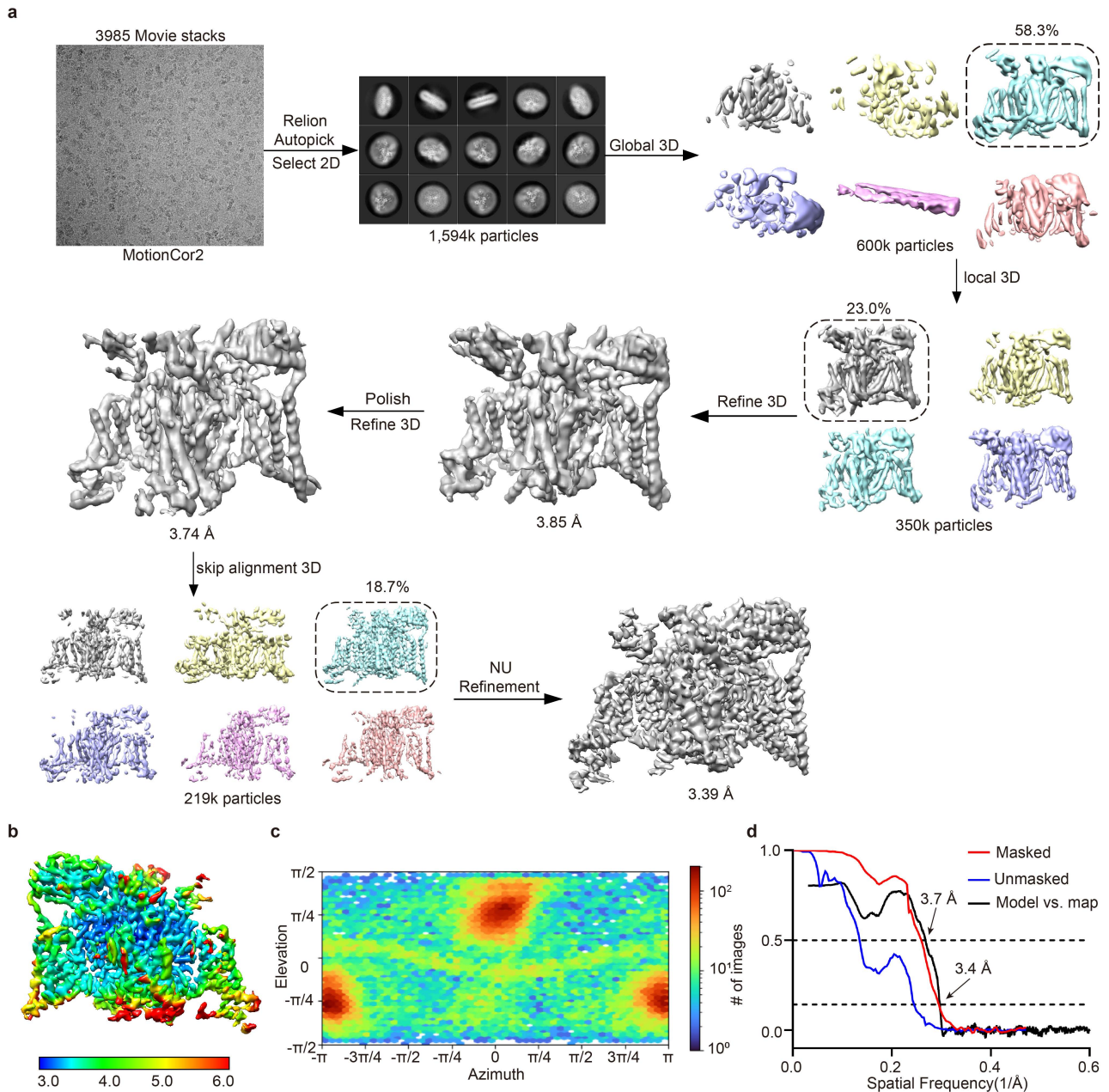
Supplementary Figure 1. Construct optimization of human $Na_v1.6/\beta1/\beta2$

a. Fluorescent SEC profiles of the $Na_v1.6$ WT and variants. The blue, red and green peaks represent signals from total protein absorbance at 280 nm, mCherry fluorescence and GFP fluorescence, respectively. Scissors indicate the truncation positions. **b-c.** Representative cryo-EM micrographs (Bar = 400 Å) and selected 2D class averages for $Na_v1.6^{WT}$ (**b**) and $Na_v1.6^{EM}$ (**c**). The experiments were repeated independently for more than 3 times with similar results.



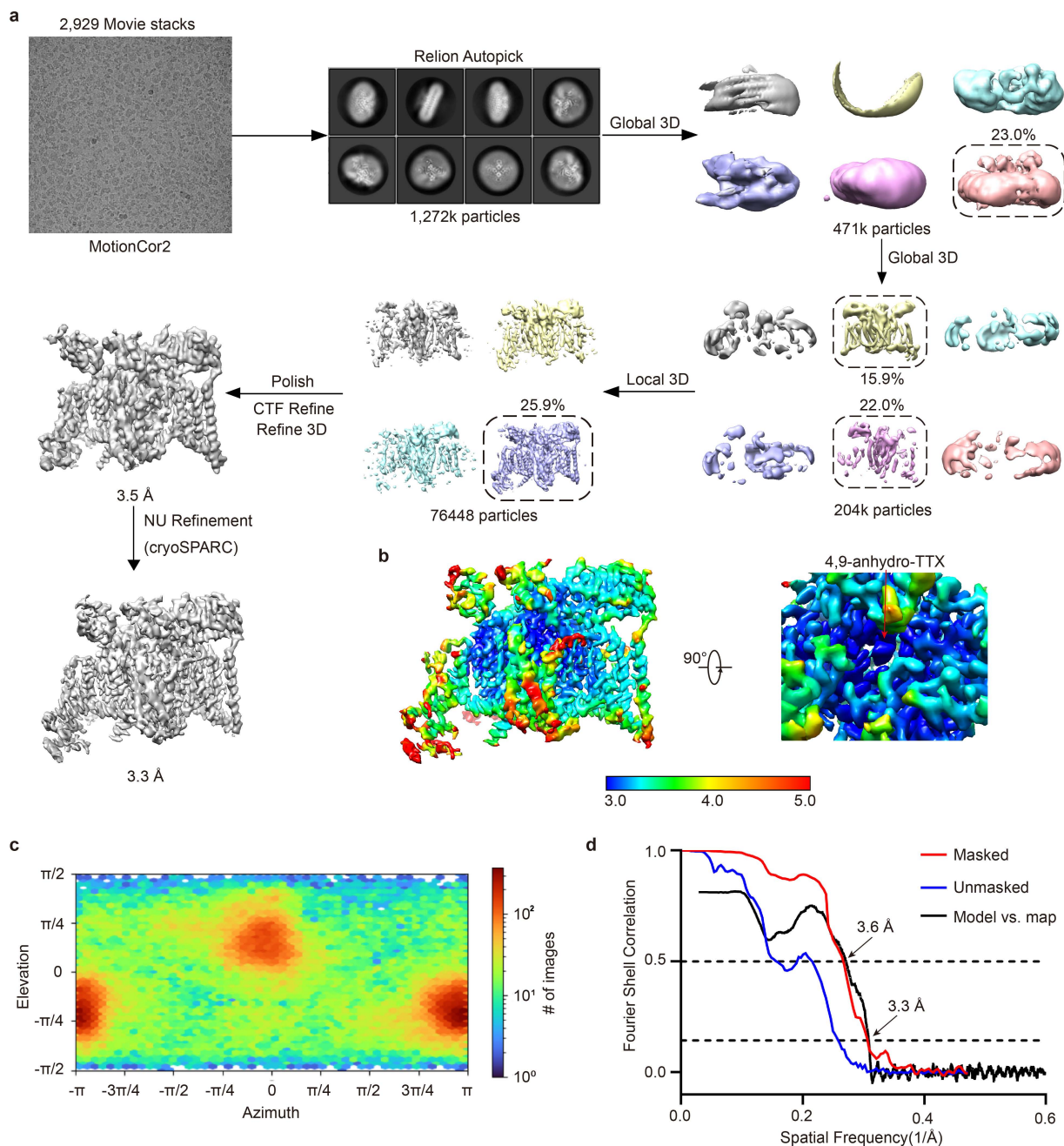
Supplementary Figure 2. Purification of human Nav1.6^{EM}/β1/β2 complex

a. SEC profile of human Nav1.6^{EM}/β1/β2 complex. Fractions between two black dashed lines were pooled and concentrated for cryo-EM analysis. **b.** SDS-PAGE gel of the purified Nav1.6^{EM}/β1/β2 sample stained by Coomassie blue. Bands for Nav1.6^{EM} and β1 were labelled. The experiments were repeated independently for more than 3 times with similar results. Source data are provided as a Source Data file.



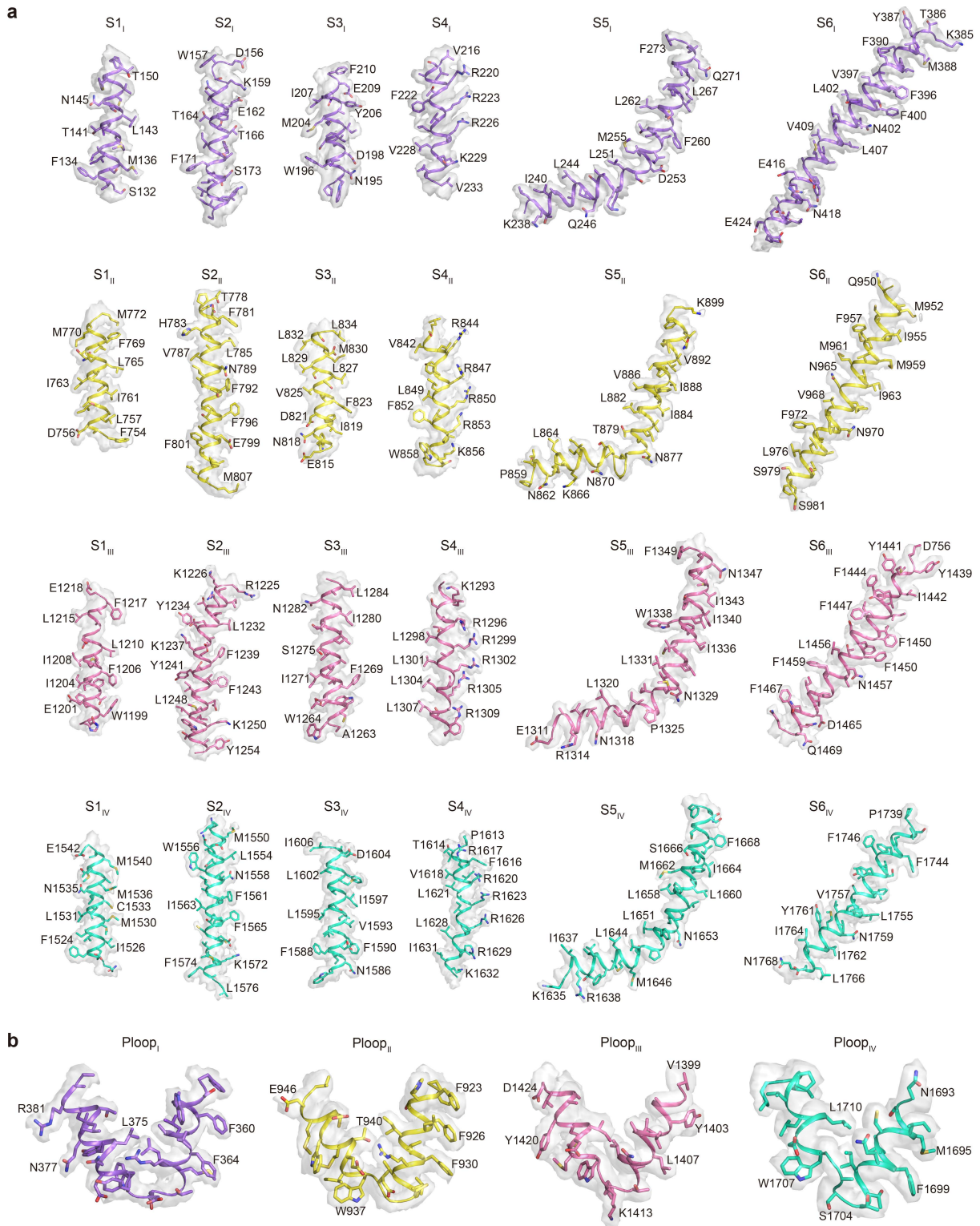
Supplementary Figure 3. Cryo-EM data processing of human Nav1.6^{EM}/β1/β2 complex

a. The flowchart of cryo-EM data processing for Nav_v1.6^{EM}/β1/β2 complex. A total of 1,594k particles were picked from 3,985 micrographs. Two rounds of 2D classification and two rounds of 3D classification were performed to remove bad particles, followed by AutoRefine, Bayesian polish and contrast transfer function (CTF) refinement in Relion to improve the map quality. The final EM density map was generated by the non-uniform (NU) refinement in CryoSPARC. **b.** Local resolution distribution of the final map of the Nav_v1.6^{EM}/β1/β2 complex. **c.** Angular distribution of the cryo-EM reconstruction of Nav_v1.6^{EM}/β1/β2 complex used for final refinement. **d.** Fourier shell correlations (FSC) curves of the Nav_v1.6^{EM}/β1/β2 complex.



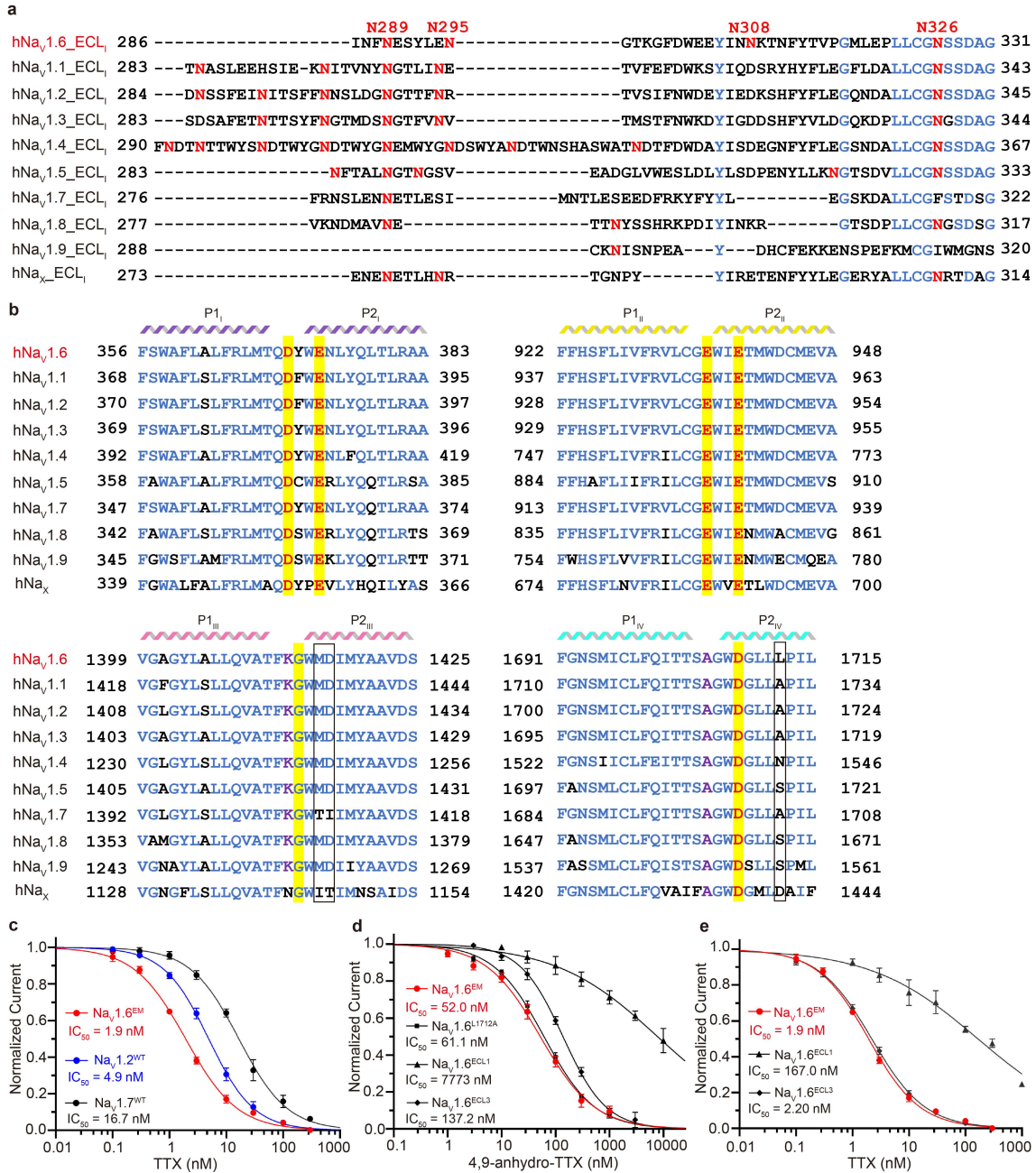
Supplementary Figure 4. Cryo-EM data processing of the Nav1.6^{EM}/β1/β2 and 4,9-ah-TTX complex

a. The flowchart of the Nav1.6^{EM}/β1/β2 and 4,9-ah-TTX complex data processing. A total of 1,272k particles were picked from 2,929 micrographs. Two rounds of global 3D classification and a further round of local 3D classification were performed to remove bad particles, followed by AutoRefine, Bayesian polish and contrast transfer function (CTF) refinement in Relion to improve the map quality. The final EM density map was generated by the non-uniform (NU) refinement in CryoSPARC. **b.** Local resolution distribution of the final 3D map. The EM density of 4,9-anhydro-TTX was labelled with a red arrow. **c.** Angular distribution of the particles used for the final 3D reconstruction. **d.** Fourier shell correlations (FSC) curves of the Nav1.6^{EM}/β1/β2 and 4,9-ah-TTX complex.



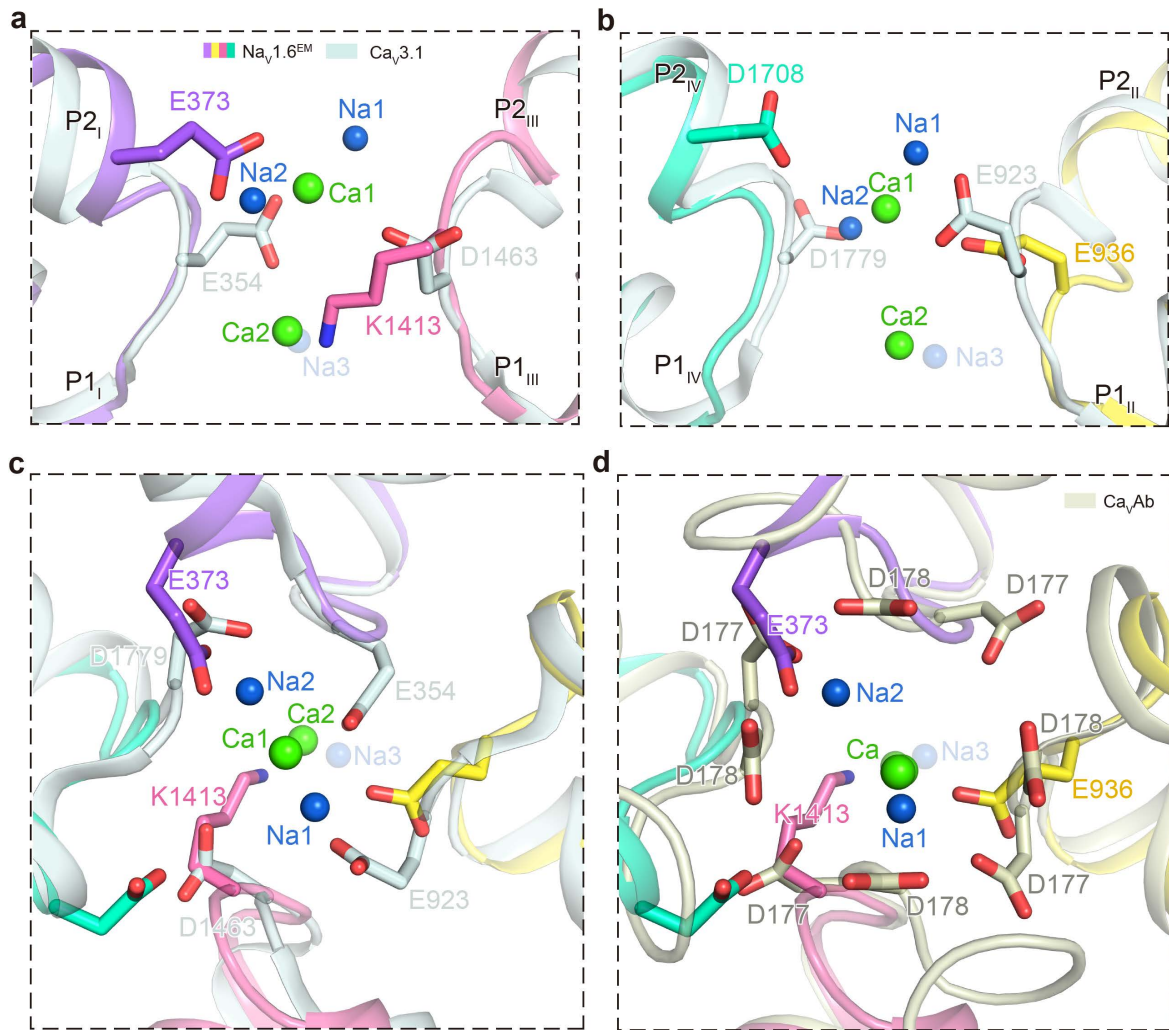
Supplementary Figure 5. Representative EM densities for Nav1.6^{EM}/β1/β2 complex.

a. The EM densities for the S1–S6 segments in each domain were shown as gray surface. **b.** The EM densities for the Pore loop segments in each domain were shown as gray surface. Side-chains of selected residues were shown as sticks.



Supplementary Figure 6. Sequence alignments of the human Na_v channels and functional characterizations of human Na_v channels by TTX analogs.

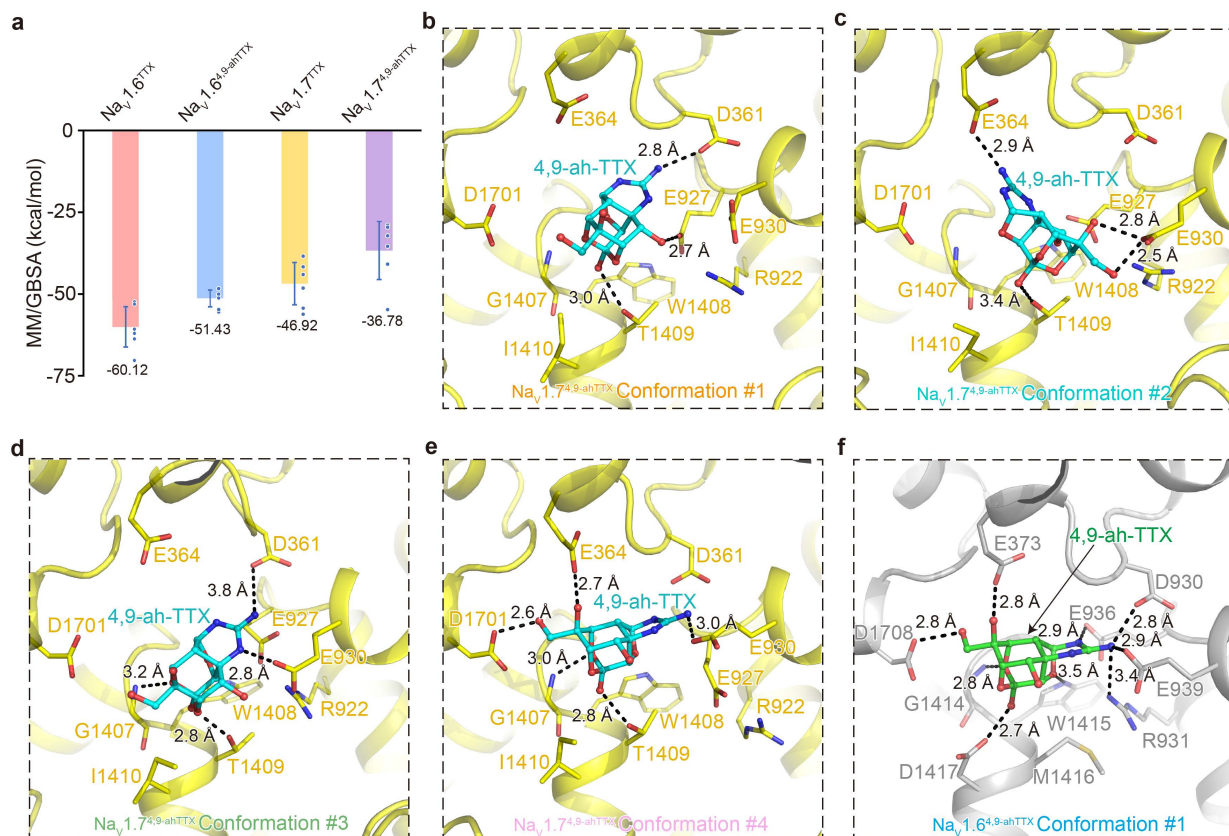
a. Sequence alignment of the ECL₁ between human Na_v channel subtypes. The identical residues were marked in blue. Asn linked glycosylation sites were marked in red and labelled. **b.** Sequence alignment of P1 and P2 of human Na_v channels. The main residues involved in 4,9-ah-TTX binding are highlighted in yellow. Positively charged residues and Lys/Ala were marked in red and purple, respectively. **c.** The concentration-response curves for the blockade of Na_v1.6^{EM} (red), Na_v1.2^{WT} (blue), and Na_v1.7^{WT} (black) by TTX. Na_v1.6^{EM}, $n = 5$; Na_v1.2^{WT}, $n = 5$; Na_v1.7^{WT}, $n = 4$. **d.** The concentration-response curves for the blockade of Na_v1.6^{EM} and its variants by 4,9-ah-TTX. Na_v1.6^{EM}, $n = 5$; Na_v1.6^{L1712A}, $n = 4$; Na_v1.6^{ECL1}, $n = 5$; Na_v1.6^{ECL3}, $n = 4$. **e.** The concentration-response curves for the blockade of Na_v1.6^{EM} and its variants by TTX. Na_v1.6^{EM}, $n = 5$; Na_v1.6^{ECL1}, $n = 7$; Na_v1.6^{ECL3}, $n = 4$. Data are presented as mean \pm SEM. n biological independent cells. Source data are provided as a Source Data file.



Supplementary Figure 7. Structural comparison of Na⁺ binding sites of Nav_{1.6}^{EM} and Ca²⁺ binding sites of Cav_{3.1}.

a-b. Side view of the Na⁺ sites compared with the Ca²⁺ sites of Cav_{3.1} (PDB code: 6KZO, colored in light blue). The diagonal repeats of DI and DIII (**a**), DII and DIV (**b**) are shown separately for clarity.

c-d. Top-down view of the Na⁺ sites of Nav_{1.6} compared with the Ca²⁺ sites of Cav_{3.1} (PDB code: 6KZO, colored in light blue) (**c**) and that of CavAb (PDB code: 4MS2, colored in gray) (**d**), respectively. Key residues were shown side-chains in sticks. Ions were shown as spheres.



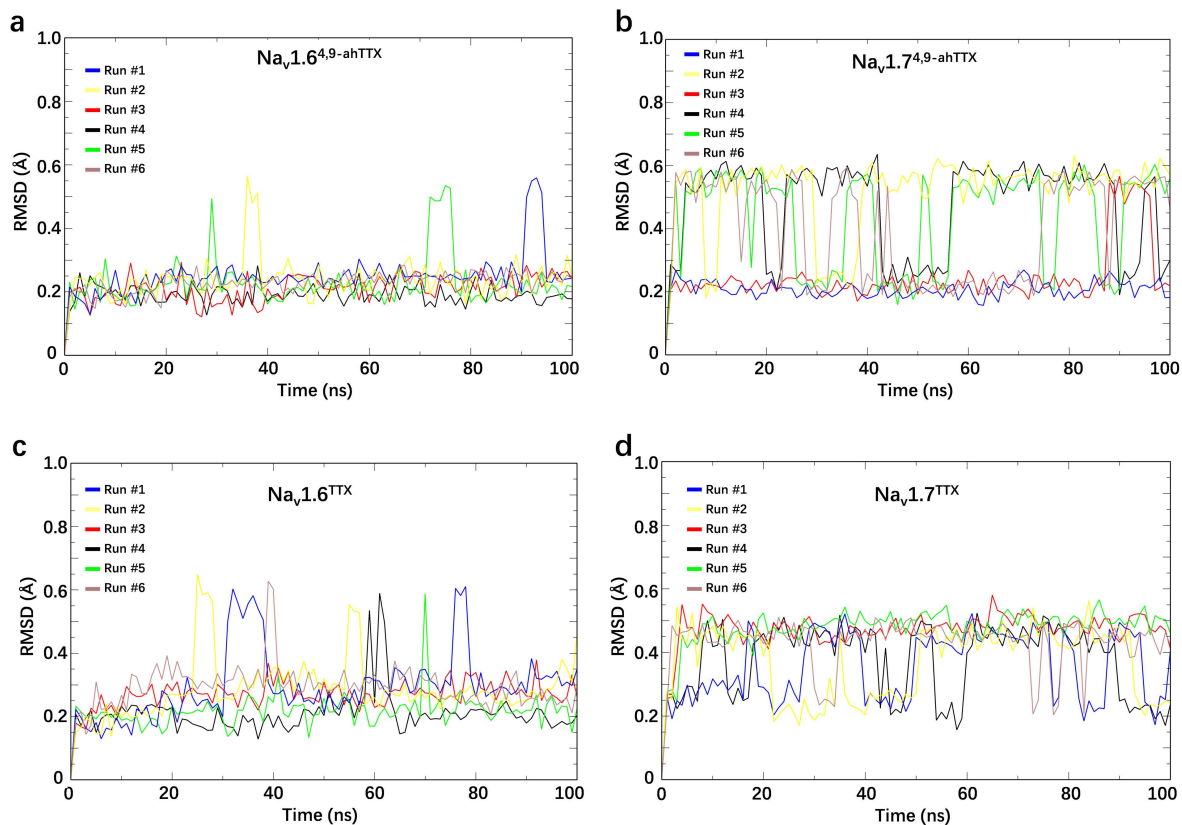
Supplementary Figure 8. Different conformations of 4,9-ah-TTX binding to Nav1.6 and Nav1.7 from MD.

a. The binding affinity of TTX and 4,9-ah-TTX to Nav1.6 and Nav1.7 calculated by MM/GBSA from the MD simulations. MD simulations for Nav_v1.6^{TTX}, Nav_v1.6^{4,9-ahTTX}, Nav_v1.7^{TTX}, and Nav_v1.7^{4,9-ahTTX} were repeated 6 times independently. Data are presented as mean ± SEM. **b-e.** Detailed binding modes of the four major conformations of 4,9-ah-TTX binding in Nav1.7 from the MD simulations. **f.** The only major binding mode of 4,9-ah-TTX in Nav1.6 from the MD simulations. Source data are provided as a Source Data file.

Residues interacting with ligands	N a _v 1.6 ^{4,9} -ahTTX		N a _v 1.7 ^{4,9} -ahTTX					N a _v 1.6 ^{TTX}				N a _v 1.7 ^{TTX}					
	c.1	c.2	c.1	c.2	c.3	c.4	c.5	c.1	c.2	c.3	c.4	c.1	c.2	c.3	c.4		
	Cluster	population (ns)	599	2	342	105	82	67	5	555	32	11	2	479	87	30	3
P [GLU936 GLU927]]	100%	100%	87%	97%	100%	28%	60%	100%	84%	100%	100%	100%	100%	100%	100%	100%	100%
HA [GLU936 GLU927]]	100%	100%	71%	98%	80%	22%	80%	92%	9%	91%	100%	100%	100%	100%	100%	100%	100%
HA [GLU373 GLU364]]	100%	100%	55%	48%	7%	97%	60%	100%	100%	82%	50%	100%	100%	100%	100%	100%	100%
P [GLU939 GLU930]]	98%	100%	21%		87%	78%		91%	34%	73%	100%	39%	76%	43%	33%		
P [ASP370 ASP361]]	97%	100%	53%	1%	91%	100%	20%	100%	100%	100%	100%	100%	100%	100%	100%	100%	100%
HA [ASP370 ASP361]]	96%	100%	52%	1%	80%	100%		100%	100%	100%	100%	98%	100%	100%	100%	100%	100%
HA [GLU939 GLU930]]	93%	50%	46%	91%	91%	78%	100%	92%	31%	82%	100%	62%	70%	73%	67%		
HD [MET1416 THR1409]]	92%	100%	92%	54%	100%	97%	80%	99%	100%	100%	100%	100%	100%	100%	100%	100%	100%
HD [ASP1417 LE1410]]	79%	100%	30%		60%	60%		25%	100%	18%		65%	18%	70%	100%	100%	100%
HD [GLY1414 GLY1407]]	75%	100%	92%	5%	98%	100%	20%	41%	100%	55%	100%	100%	100%	100%	100%	100%	100%
HA [ASP1417 LE1410]]	73%	50%						20%	100%	9%							
HD [TRP1415 TRP1408]]	65%	50%	45%	10%	24%	97%	60%	46%	100%	45%		84%	85%	70%	67%		
AR [TYR371 TYR362]]	54%		21%	53%		61%	60%	32%	6%	9%		8%	15%				
HA [ASP1708 ASP1701]]	51%	100%	37%		9%	99%		52%	100%			37%	54%	30%			
HD [ARG931 ARG922]]	47%	50%	48%	65%	45%		80%	10%		9%		53%	2%	87%	100%		
HY [TYR371 TYR362]]	39%	50%	58%	82%		30%	60%	37%	9%	18%		23%	24%	7%			
HD [GLY1706 GLY1699]]	12%		1%					36%	22%	18%		71%	84%	80%	100%		
HA [GLY1414 GLY1407]]	11%	50%	0%					19%	3%	18%							
HA [PHE1412 PHE1405]]	5%		16%	27%				4%	31%	9%		11%	11%	20%			
HD [GLY1709 GLY1702]]	5%	50%						23%		9%							
P [GLU373 GLU364]]	5%		38%	54%	20%		60%	34%		9%		73%	2%	100%	100%		
HY [LYS1413 LYS1406]]	1%																
HA [GLY1706 GLY1699]]	1%							5%									
HA [TYR371 TYR362]]	1%		7%				40%	1%		50%		2%	1%				
HD [TYR371 TYR362]]	0%		3%					65%	100%	91%	100%	21%	91%	3%			
HD [ASN374 ASN365]]	0%							4%									
HD [TRP1707 TRP1700]]	0%																
HA [GLY317 GLY308]]			1%														
HD [LEU319 LYS310]]			2%	6%								0%					
HA [GLN369 GLN360]]			5%			7%	20%	1%	16%			1%	9%				
HA [CYS934 CYS925]]			1%			1%											
HA [GLY935 GLY926]]			47%			93%						1%	16%				
HD [LYS1413 LYS1406]]			1%					10%	100%			19%	57%				
AR [TRP1415 TRP1408]]			1%	3%													
HA [MET1416 THR1409]]			78%	6%	100%	97%		0%				99%	100%	100%	100%		
P [ASP1708 ASP1701]]			13%	1%								0%					
HA [THR314 TYR305]]				1%													
HD [TRP917 TRP908]]				4%			20%										
HD [TYR1420 TYR1413]]				21%			60%										
HD [TRP372 TRP363]]								5%		9%							
HA [LYS1413 LYS1406]]								20%		27%							

Supplementary Figure 9. Ligand-protein contact analysis based on MD study.

The type and frequency of interactions between protein and ligand are listed for each conformation cluster of a protein-ligand system. C.# indicates the index of the cluster. The digits associated with green-white color scheme indicate the appearance frequency of the interaction within the cluster. For residues interacting with ligands, the annotation follows the format of “Interaction Type [Residue in Na_v1.6 (Counterpart the residue in Na_v1.7)]”. The interaction identification and interaction type definition follow the study described by Daria et al¹. A general annotation for interaction types is listed below: IP (salt bridges), HY (hydrophobic interactions), HA (hydrogen bond, ligand atom as acceptor), HD (hydrogen bond, ligand atom as donor), AR (aromatic system related stacking).



Supplementary Figure 10. Ligand dynamics in MD study.

a to **d**, The ligand RMSD plots for each replicate of the simulations for $\text{Nav}1.6^{4,9}\text{-ahTTX}$ (**a**), $\text{Nav}1.7^{4,9}\text{-ahTTX}$ (**b**), $\text{Nav}1.6^{\text{TTX}}$ (**c**), and $\text{Nav}1.7^{\text{TTX}}$ (**d**). Before RMSD calculation, all the structures in each trajectory were aligned with the initial structure of that trajectory by using Least Squares algorithm.

Supplementary Table 1. Concentration-response inhibition statistics of 4,9-ah-TTX or TTX for different subtypes and variants.

Human subtypes	Compounds	IC50 (nM)	95% CI	n
Nav1.6 ^{EM}	4,9-ah-TTX	52.0	44.33 to 61.09	5
Nav1.2 ^{WT}	4,9-ah-TTX	257.9	217.4 to 305.9	6
Nav1.7 ^{WT}	4,9-ah-TTX	1340	1209 to 1486	6
Nav1.6 ^{ELC1}	4,9-ah-TTX	7773	4538 to 13313	5
Nav1.6 ^{ELC3}	4,9-ah-TTX	137.2	123.1 to 152.9	4
Nav1.6 ^{L1712A}	4,9-ah-TTX	61.1	55.45 to 67.23	4
Nav1.6 ^{M1416T/D1417I}	4,9-ah-TTX	256.5	224.0 to 293.7	5
Nav1.6 ^{EM}	TTX	1.9	1.76 to 2.13	5
Nav1.2 ^{WT}	TTX	4.9	4.43 to 5.46	5
Nav1.7 ^{WT}	TTX	16.7	14.54 to 19.18	4
Nav1.6 ^{ELC1}	TTX	167.0	115.2 to 242.3	7
Nav1.6 ^{ELC3}	TTX	2.2	2.01 to 2.41	4

Supplementary Table 2. Primers used in this study.

Name	Sequence (5' to 3')
Nav1.6 F	atggcagcgcggctgcttg
Nav1.6 R	acacttggattctctgacctcttttgt
Nav1.6 ^{ΔDI-DII} F	tcccctcggagctctcgggaaggacagaatcaacagtata
Nav1.6 ^{ΔDI-DII} R	gattctgtccttccgagagctccgaggggagccccctcc
Nav1.6 ^{ΔDII-DIII} F	acagaggatgttagcggcaagtcttggtgatcctgcgg
Nav1.6 ^{ΔDII-DIII} R	ccaccaagacttgcgctaacaatcctctgtgttgaggtt
Nav1.6 ^{ΔCTer} F	caccgggagaaaaaagagctggaagttctgttccaggggcccattggtgagcaa
Nav1.6 ^{ΔCTer} R	ctggaacagaactccagctctttttctcccgggtgtgtgcctccattctccagc
Nav1.6 ^{L1712A} F	gatggcctgctgGCGcccatcctaaaccgccccctgact
Nav1.6 ^{L1712A} R	ggtttaggatgggCGCcagcaggccatccaaccagctga
Nav1.6 ^{ECL1} F	ctgcagctgtcatggggaaccttaagcataaatgtttcgaattca
Nav1.6 ^{ECL1} R	agtgtaaaaacttgtaaccataatcagggtttctgccaattttcac
Nav1.6 ^{ECL3} F	ttcagcatcatgggagttaactgtttgctggcaagttctatgagtg
Nav1.6 ^{ECL3} R	aagaaggccaggtatcctgccccgacattatcaaagttcactttcag
Nav1.6 ^{M1416T/D1417I} F	cctcaaaggctggacgattatcatgtatgcagctgtagattcccgggaagcctg
Nav1.6 ^{M1416T/D1417I} R	cagctgcatacatgataatcgtccagcctttgaaggttgctactgaagaagggc

Supplementary Table 3. Cryo-EM data collection, refinement and validation statistics

	Nav1.6 ^{EM} /β1/β2 (EMDB-34387) (PDB: 8GZ1)	Nav1.6 ^{4,9-ahTTX} (EMDB-34388) (PDB: 8GZ2)
Data collection and processing		
Magnification	130,000 ×	130,000 ×
Voltage (kV)	300	300
Electron exposure (e ⁻ /Å ²)	60	60
Defocus range (μm)	-1.2 ~ -2.2	-1.2 ~ -2.2
Pixel size (Å)	1.04	1.04
Symmetry imposed	C1	C1
Initial particle images (no.)	1594472	1272486
Final particle images (no.)	41387	76448
Map resolution (Å)	3.4	3.3
FSC threshold	0.143	0.143
Map resolution range (Å)	3.0 ~ 5.0	3.0 ~ 5.0
Refinement		
Initial model used (PDB code)	6J8I	Nav1.6-β1-β2
Model resolution (Å)	3.7	3.6
FSC threshold	0.5	0.5
Map sharpening <i>B</i> factor (Å ²)	-69.0	-58.1
Model composition		
Non-hydrogen atoms	11912	11984
Protein residues	1445	1467
Ligands	19	18
<i>B</i> factors (Å ²)		
Protein	90.46	79.36
Ligand	98.52	75.52
R.m.s. deviations		
Bond lengths (Å)	0.003	0.005
Bond angles (°)	0.623	0.818
Validation		
MolProbity score	1.89	2.03
Clashscore	10.55	12.37
Poor rotamers (%)	0.00	0.00
Ramachandran plot		
Favored (%)	94.98	93.62
Allowed (%)	5.02	6.38
Disallowed (%)	0.00	0.00

SUPPLEMENTARY REFERENCES

- 1 Kokh, D. B. *et al.* A workflow for exploring ligand dissociation from a macromolecule: Efficient random acceleration molecular dynamics simulation and interaction fingerprint analysis of ligand trajectories. *J Chem Phys* **153** (2020).